symmetry

MDPI

Article

Analytical Study of the Energy Loss Reduction during Three-Dimensional Engine Oil-Based Hybrid Nanofluid Flow by Using Cattaneo–Christov Model

Ramadan A. ZeinEldin [1], Asad Ullah [2,*], Hamiden Abd El-Wahed Khalifa [3,4] and Muhammad Ayaz [5]

[1] Deanship of Scientific Research, King Abdulaziz University, Jeddah 21589, Saudi Arabia
[2] Department of Mathematical Sciences, University of Lakki Marwat, Lakki Marwat 28420, Khyber Pakhtunkhwa, Pakistan
[3] Department of Operations and Management Research, Faculty of Graduate Studies for Statistical Research, Cairo University, Giza 12613, Egypt
[4] Department of Mathematics, College of Science and Arts, Qassim University, Al-Badaya 51951, Saudi Arabia
[5] Department of Mathematics, Abdul Wali Khan University Mardan, Mardan 23200, Khyber Pakhtunkhwa, Pakistan
* Correspondence: asad@ulm.edu.pk

Abstract: In this work, we analyzed the hybrid nanofluid (Ag+CuO+kerosene oil) flow past a bidirectionally extendable surface in the presence of a variable magnetic field. The hybrid nanofluid flow considered is electrically conductive and steady. For the simulation of the problem, the Cattaneo–Christov double-diffusion (CCDD) model was considered, which generalizes Fourier's and Fick's laws. The impact of the Hall current produced was taken into account. The physical problem was transformed into a mathematical form with the help of suitable transformations to reduce the complexity of the problem. The transformed system of coupled ordinary differential equations (ODEs) was solved with the semi-analytical method. The results are plotted in comparison with the ordinary nanofluid (CuO+kerosene oil) and hybrid nanofluid (Ag+CuO+kerosene oil). The impact of various parameters $(Pr, Sc, \gamma_0, m, M, Nb, Nt, \epsilon_1, \epsilon_2)$ on the state variables is described. The velocity gradient under the impact of the mass flux and magnetic parameter shows a decreasing behavior, while the Hall parameter and the stretching ratio show an increasing behavior. Moreover, the skin friction, rate of heat, and mass transfer are numerically displayed through tables. In this work, we found that the thermal and concentration relaxation coefficients showed a decreasing behavior for their increasing trends. For the validation of the implemented technique, the squared residuals are computed in Table 2, which shows that the increasing number of iterations decreases the squared residual error. The results show that Ag+CuO+kerosene oil has good performance in the reduction of the heat transfer rate.

Keywords: symmetric flow; hybrid nanofluid; energy loss; heat and mass transfer; Cattaneo–Christov model; stretching surface; homotopy analysis method

Citation: ZeinEldin, R.A.; Ullah, A.; Khalifa, H.A.E.-W.; Ayaz, M. Analytical Study of the Energy Loss Reduction during Three-Dimensional Engine Oil-Based Hybrid Nanofluid Flow by Using Cattaneo–Christov Model. *Symmetry* **2023**, *15*, 166. https://doi.org/10.3390/sym15010166

Academic Editors: Amin Amiri Delouei, Hasan Sajjadi and Meysam Atashafrooz

Received: 8 December 2022
Revised: 27 December 2022
Accepted: 4 January 2023
Published: 6 January 2023

1. Introduction

In the last few years, the applications of heat transfer in different fields (engineering and technology) have attracted many researchers. One such important application is the nature of the electronic devices used, where the thermal conductivity is very low, due to the ordinary mixtures (ethylene glycol, water, oil, etc.). However, now, almost every researcher has access to increase the thermal conductivity of these fluids (materials). This is thanks to Choi and Eastman [1,2], who introduced the idea by the mixing of small-sized particles (having a size below 100 nm) with the available fluid. This available fluid is known as the base fluid, while the mixture formed by a single-type mixing procedure is known as the nanofluid. This new mixture formed has many physical advantages over the ordinary fluid.

This procedure opened the door to a new era in the field of fluid mechanics. Initially, this work looked to be not very interesting, but as time passed, this work has put the interest of the researchers on a single track. Currently, two different techniques are used for the preparation of these nanofluids. These fluids can be prepared at the laboratory, as well as at the industry level. Maiga et al. [3] conducted a numerical simulation of the nanofluid's behavior. They estimated the heat transfer increase of the nanofluid in an evenly heated tube under turbulent and laminar flow conditions and employed approximated correlations for the experimental data. They reported that the increasing value of the Reynolds number in the turbulent case increases the transfer of heat. This rapid increase was found to be due to the dimension of the nanoparticles used in the formation of the nanofluid. A new theoretical model for nanoliquids' behavior through an expanding surface was analyzed by Khan and Pop [4]. In this work, they reported the stabilization of the stream and thermal behavior. The magnetohydrodynamics (MHD) mixed convective stagnation point flow of a micro-polar nanoliquid was performed by Seth et al. [5]. They used a new empirical relation for this study and implemented the successive linearization method for solution purposes. The study of nanofluids subject to different conditions and geometries can be found in [6–8].

Researchers are always trying to investigate problems and find a feasible and suitable solution. In light of the above literature, researchers have taken keen interest in advancing the existing work to a next level. In the preparation of nanofluids instead of single-element nanoparticles, two or more than two nanoparticles of different elements are used. Therefore, a single-type nanoparticle is replaced with a hybrid one. These nanofluids have various applications in agriculture production, applied and biological sciences, and material sciences. These are accessible with a very low cost and have many applications in the transfer of heat and other coolant projects. On the other hand, the advantages of these fluids include increased thermal conductivity, good transfer of heat, and other physical significance. Due to these properties, they are used for coolant purposes to increase efficiency and reduce energy loss. In 2007, for the first time, Jana et al. [9] investigated the thermal conductivity of hybrid nanofluids. They performed a comparative survey with a single-phase common nanofluid, where they found a remarkable increase in the transfer of heat for computing the thermal conductivity of the hybrid nanofluid. Madhesh et al. [10] studied a copper-titanium hybrid nanofluid to analyze the rheological characteristic, as well as the transfer of heat. In this work, in the preparation of the hybrid nanofluid, 55nm particles with concentrations varying from 0.1 vol.% to 2.0 vol.% were used. In the experiment, a 52% increase in the coefficient of the convective heat, a 49% increase in the Nusselt number, an average increase of 68% in the coefficient of heat transfer, and a 1.0% increase in the volume concentration were observed. Later on, in 2010, Ho et al. [11] performed an investigation of the increase of the thermal conductivity by utilizing a water-based hybrid nanofluid having a microencapsulated phase change material (MEPCM) and Al_2O_3 nanoparticles. In this work, higher thermal conductivity and concentration as compared to the phase change materials (PCMs) were reported. Suresh et al. [12] studied the nanoparticles' concentration effect over the thermal conductivity for the hybrid nanofluid Al_2O_3-Cu/water. In this study, for synthesis purposes, the two-step method was implemented. Labib et al. [13] considered the Al_2O_3–CNT/water nanofluid and studied the impact of the Reynolds number and the nanoparticles' concentration for the transfer of heat. They reported that the increase of Al_2O_3 and carbon nanotubes (CNTs) inside the medium increased the thermal conductivity. In this work, the concentration of the nanoparticles increased the transfer of heat coefficient and work, in addition to the friction factor. The Al_2O_3-Cu/water hybrid nanofluid flow by considering the forced convection was utilized by Moghadassi et al. [14]. Both single- and two-phase analysis were performed for synthesis purposes, and both phases were analyzed. They reported a 4.73% increase in the single-phase model, while 13.46% in the two-phase model for the hybrid nanofluid in comparison with water. Furthermore, a 4% increase in the Nusselt number for the two-phase model was observed.

In recent years, various uses for electrically conducting fluid and MHD boundary flow have been reported in engineering and industry [15]. Similar applications of the MoS2 nanoparticles for the MHD slip flow were reported by Khan [16]. His results showed the heat transfer increase for the MoS2 nanoparticles. Chamkaa et al. [17] analyzed the Cu-water nanofluid filled square cavity and studied the mixed convection with the impact of the magnetic field. The mathematical problem was tackled with the finite-difference method. The results were presented for the inclination angle, the Hartmann and Richardson parameters, and the nanofluid volume fraction under the impact of the applied magnetic field. Alsabery et al. [18] considered the two-phase Buongiorno model for the square enclosure in the mixed convection of Al_2O_3-water nanofluid flow with the impact of the magnetic field. Various obstacles (circular, triangular, and square) were assumed inside the cavity. The Galerkin method was employed for the solution of the problem, and the results were presented in the form isotherms and streamlines. They found that the heat produced inside the cavity was higher for the triangular obstacles compared to the others. Ellahi [19] showed that the velocity profile decreased with the variation in the MHD parameter for the non-Newtonian MHD fluid flow inside a pipe. The pipe was considered at a higher temperature compared to the fluid flowing through it. Explicit expressions for the state variables were derived with the semi-analytical method, the HAM. Sheikholeslami et al. [20] reported the MHD fluid flow inside a permeable channel. They found that, with the increasing values of the Hartmann number, the velocity boundary layer declined, while on the other hand, the boundary layer thickness decreased with the increasing values of the Reynolds number and volume fraction. Seyyedi et al. [21] used the ANSYS Fluent software and the control volume finite-element method for the natural convection MHD fluid flow through a semi-annulus enclosure. In their study, they reported the entropy generation due to the MHD flow. In this work, they showed that the entropy generation decreased for various pertinent parameters. Rashidi et al. [22] studied the entropy generation and the second law of thermodynamics for the MHD nanofluid flow inside a porous rotating disk. In this study, the applications of the rotating disk with entropy generation were presented. In the investigation of the MHD (three-dimensional) 3D flow for the Lorentz force impact over the temperature profile, Sheikholeslami and Ellahi used the lattice Boltzmann method (LBM) [23]. The viscosity and thermal conductivity were calculated with the correlation model, Koo–Kleinstreuer–Li (KKL). The generation of the entropy and heat transfer both were reported to decline with the increasing values of the Rayleigh parameter, while the opposite behavior was reported for the Hartmann parameter. Recently, Biswas et al. [24] studied the application of Cu-water nanofluid inside a square cavity, where the left wall was considered hot. The problem was solved with the finite-volume method, and various parameters' impacts were studied. The wavy wall and convection impacts were studied in detail. The bio-convection impacts over the heat and mass transfer were reported for cleaner energy and bio-cell production. Manna et al. [25] reported the entropy generation and Lorentz forces' impact inside a quarterly squared cavity. The work was carried out for various dimensionless parameters, where the results described with the practical applications of energy storage, the cooling of electronic devices, and other food and technological purposes. Biswas et al. [26] also reported partial magnetic impacts on the nanoliquid flow past a porous medium numerically. The magnetic field impact showed a 17.15% or 9.71% decline in the heat transfer rate. More recent studies of the flow inside a square cavity can be found in [27–30].

The boundary layer flow over different geometries and, especially, in the case of a stretching sheet has been analyzed by various researchers. The role of this type of flow is encountered in wire drawing, copper wire tinning, metallurgy, glass fiber, rubber and plastic sheets, glass blowing, etc. The basic idea of the boundary layer flow was presented by Sakiadis [31–33] in the case of a solid surface motion at a fixed speed. This idea was further utilized by Crane [34] for a two-dimensional (2D) flow past a stretching sheet. The scientist continued their work on this new idea and extended the work further to other physical constraints [35,36]. The boundary layer flow past an exponentially

stretchable sheet by considering the suction and injection of the sheet for the heat and mass transfer analysis was utilized by Magyari et al. [37]. In the boundary layer flow analysis, the shrinking and stretching sheet caused the flow to move back and forth towards the origin. This unusual behavior was reported by Wang [38] for the first time by analyzing the liquid film's unsteady flow past a stretching sheet. The exact solution of the Navier–Stokes equations for a stretching sheet was presented by Miklavcic and Wang [39]. They also reported that the stability of the flow over the sheet requires the suction of mass. Bhattacharyya [40] investigated fluid flow and heat transfer across an exponentially shrinking sheet. Their findings showed that the feasibility of the steady flow depends on the mass suction parameter when exceeding a specific critical value. In another study, Bhattacharyya et al. [41] examined the stagnation point flow and heat transfer across a sheet subject to exponential shrinkage. Bachok et al. [42] examined the steady two-dimensional stagnation point flow of an aqueous nanofluid over an exponentially stretching/shrinkage surface. A substantial amount of research has been dedicated to the analysis of fluid flow across the exponentially stretching/shrinking plate. Some recent examples are mentioned here [43–46].

The Buongiorno nanoliquid model is modified with the help of the Oldroyd convection time derivative to obtain the Cattaneo–Christov model [47]. This modification is mainly concerned with the Fourier–Fick laws [48]. Zheng and Zhang [49] investigated the Maxwell nanofluid flow past a stretching sheet by considering the heat and mass transfer together with the slip effects. They used the Cattaneo–Christov double-diffusion (CCDD) model in their analysis. Hayat et al. [50] studied the steady, 3D, and bidirectional Newtonian fluid flow by considering the CCDD model. In the very next year, Hayat et al. [51] analyzed analytically the viscoelastic nanofluid flow by considering the CCDD model. Recently, Hayat et al. [52,53] investigated the CCDD model for the Prandtl and Walters-B fluids by considering the heat source/sink and chemical reaction effects past an expanding surface. The Eyring–Powell nanomaterial was analyzed by Ibrahim [54] considering the CCDD model for the flow over a bidirectionally expanding sheet. More recent surveys of the Cattaneo–Christov model can be found in [55–58]. From the literature, it is clear that the impact of the Hall current on the CCDD model with a variable magnetic field has not been reported for the hybrid nanofluid Ag+CuO+kerosene oil.

This work aimed to analytically investigate the hybrid nanofluid flow based on kerosene oil past a bidirectionally expanding surface in the presence of a variable magnetic field. The nanofluid flow considered is electrically conductive and steady. For the exploration and modeling of the physical problem, the CCDD model was used for the optimal solution. Moreover, the current produced due to the magnetic parameter was also counted in the physical problem. In this article, Section 2 is devoted to the problem description and physical geometry with a detailed mathematical description. In Section 3, the analytical method used is described in detail with residual error analysis, and in Section 4, the results obtained are described and discussed in detail. Finally, the discussion of the tables and conclusions are presented in Sections 5 and 6, respectively.

2. Mathematical Model of the Problem

Consider a steady, bidirectional and incompressible flow of a hybrid nanofluid (Ag+CuO+kerosene oil) over an extendable surface. The geometry of the problem was chosen in the Cartesian coordinate system, centered at $(x, y, z) = (0, 0, 0)$, as can be seen in Figure 1 [50]. The geometry of the problem was chosen in such away that the $u_w = c \exp\left(\frac{x+y}{L}\right)$ and $v_w = d \exp\left(\frac{x+y}{L}\right)$ velocities act along the x- and y-axis, respectively. The wall temperature and concentration of the hybrid nanoparticles were assumed in the exponential forms $T_w - T_\infty = T_0 \exp\left(\frac{a(x+y)}{2L}\right)$ and $C_w - C_\infty = C_0 \exp\left(\frac{a(x+y)}{2L}\right)$, respectively. A variable magnetic field $B(x, y) = B_0 \exp\left(\frac{x+y}{2L}\right)$ was applied perpendicular to the surface, where B_0 shows the strength of the applied magnetic field. The fluid is electrically conductive, in which the induced current produced was considered in the

nanofluid fluid flow. Moreover, the heat and mass transfer were investigated through the double-diffusion Cattaneo–Christov theory, which acts as a generalization of the famous Fourier and Fick laws [47,50]:

$$\tilde{q} + \Lambda_e\left(\tilde{q}_t + \tilde{V}\cdot\nabla\tilde{q} - \tilde{q}\cdot\nabla\tilde{V} + (\nabla\cdot\tilde{V})\tilde{q}\right) + k\nabla T = 0, \tag{1}$$

$$\tilde{J} + \Lambda_c\left(\tilde{J}_t + \tilde{V}\cdot\nabla\tilde{J} - \tilde{J}\cdot\nabla\tilde{V} + (\nabla\cdot\tilde{V})\tilde{J}\right) + D_B\nabla C = 0. \tag{2}$$

In Equations (1) and (2), $\tilde{q}$ and $\tilde{J}$ show the heat and mass fluxes, T and C denote the temperature and concentration, respectively, k is the thermal conductivity, $\tilde{V}$ is the velocity field, D_B is the Brownian motion parameter, and Λ_e and Λ_c describe the energy and concentration relaxation factors, respectively. By letting $\Lambda_e = 0 = \Lambda_c$, the famous Fourier and Fick laws can be obtained. Considering the steadiness condition of the nanofluid flow, we have from Equations (1) and (2) the theory, which acts as a generalization of the famous Fourier and Fick laws [47,50].

$$\tilde{q} + \Lambda_e\left(\tilde{V}\cdot\nabla\tilde{q} - \tilde{q}\cdot\nabla\tilde{V} + (\nabla\cdot\tilde{V})\tilde{q}\right) + k\nabla T = 0, \tag{3}$$

$$\tilde{J} + \Lambda_c\left(\tilde{V}\cdot\nabla\tilde{J} - \tilde{J}\cdot\nabla\tilde{V} + (\nabla\cdot\tilde{V})\tilde{J}\right) + D_B\nabla C = 0. \tag{4}$$

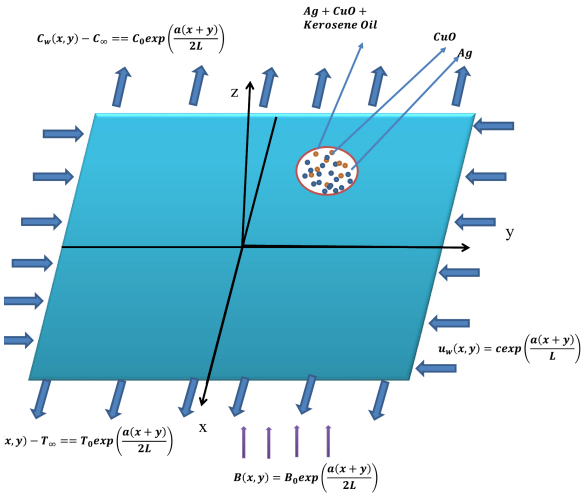

Figure 1. Geometrical description of the study.

Since we considered the nanofluid flow as electrically conductive under the impact of the applied variable magnetic parameter, after some time, the magnetic field produces a current known as the Hall current. This whole process is governed by the generalized Ohm's law given below [59–61]:

$$\tilde{j} + \frac{\omega_e}{B_0 t_e}\times(\tilde{j}\times\tilde{B}) + \frac{\sigma P_e}{e n_e} = \sigma(\tilde{E} + \tilde{V}\times\tilde{B}), \tag{5}$$

where n_e, e, σ, $\tilde{j}$, $\tilde{V}$, and B_0 describe the number density, charge of electrons, electrical conductivity and electrical current density, velocity of the fluid, and strength of the magnetic field, respectively. In light of the above assumptions, the modified Buongiorno nanofluid model for the boundary layer nanofluid flow takes the following form [52,55,62]:

$$u_x + v_y + w_z = 0, \tag{6}$$

$$uu_x + vu_y + wu_z = \nu_{hnf}u_{zz} - \frac{\sigma_{hnf}}{\rho_{hnf}}\frac{B^2}{1+m^2}(u - mv), \tag{7}$$

$$uv_x + vv_y + wv_z = \nu_{hnf} v_{zz} - \frac{\sigma_{hnf}}{\rho_{hnf}} \frac{B^2}{1+m^2}(v + mu), \tag{8}$$

$$uT_x + vT_y + wT_z = \alpha_m T_{zz} - \Phi_e \Lambda_e + \tau\left(T_z C_z + \frac{D_T}{T_\infty} T_z^2\right), \tag{9}$$

$$uC_x + vC_y + wC_z = D_B C_{zz} - \Phi_c \Lambda_c + \frac{D_T}{T_\infty} C_{zz}. \tag{10}$$

Here, in Equations (9) and (10), the terms Φ_e and Φ_c are the steady Cattaneo–Christov expressions defined as [59]:

$$\begin{aligned}\Phi_e = u^2 T_{xx} + v^2 T_{yy} + w^2 T_{zz} + 2(uvT_{xy} + vwT_{yz} + uwT_{xz}) + T_x(uu_x + vu_y + wu_z)\\ + T_y(uv_x + vv_y + wv_z) + T_z(uw_x + vw_y + ww_z),\end{aligned} \tag{11}$$

$$\begin{aligned}\Phi_c = u^2 C_{xx} + v^2 C_{yy} + w^2 C_{zz} + 2(uvC_{xy} + vwC_{yz} + uwC_{xz}) + C_x(uu_x + vu_y + wu_z)\\ + C_y(uv_x + vv_y + wv_z) + C_z(uw_x + vw_y + ww_z).\end{aligned} \tag{12}$$

Here, u, v, and w are the velocity components along the x, y, and z directions, respectively, ρ is the density, ν is the kinematic viscosity, Λ_e and Λ_c represent the relaxation time of the energy and concentration fluxes, τ is the adiabatic index, D_T represents the thermophoretic parameter, and D_B indicates the diffusion parameter of the nanoparticles. The boundary restrictions from the physical problem take the following form.

$$\begin{aligned}u = u_w(x,y), v = v_w(x,y), w = w_w(x,y) = w_0 \exp\left(\frac{x+y}{2L}\right), T = T_w, C = C_w, \text{ as } z \to 0,\\ u \to 0, v \to 0, C \to C_\infty, T \to T_\infty \text{ as } z \to \infty.\end{aligned} \tag{13}$$

where $u_w = c\exp\left(\frac{x+y}{L}\right)$ and $v_w = d\exp\left(\frac{x+y}{L}\right)$ are the bidirectional velocities along the x- and $y-axis$, respectively. Here, c and d are the references of the velocities and L is the length (characteristic) of the sheet. Introduce the following similarity variable [62]:

$$\begin{aligned}u = c\exp\left(\frac{x+y}{2L}\right)f', v = c\exp\left(\frac{x+y}{2L}\right)g', w = -\left(\frac{c\nu_f}{2L}\right)^{0.5}\exp\left(\frac{x+y}{2L}\right)(f + g + \zeta f' + \zeta g'),\\ T = T_\infty + T_0\exp\left(\frac{a(x+y)}{2L}\right), C = C_\infty + C_0\exp\left(\frac{a(x+y)}{2L}\right), \zeta = \left(\frac{c}{2\nu_f L}\right)^{0.5}\exp\left(\frac{x+y}{2L}\right),\\ T - T_\infty = (T_f - T_\infty)\theta(\zeta).\end{aligned} \tag{14}$$

Here, the prime shows the derivative with respect to ζ and $w_0 = -\left(\frac{c\nu_f}{2L}\right)^{0.5} S_0$, where S_0 represents the dimensionless flux of the mass, which further explains the suction/injection.

Equations (6)–(10) together with the boundary conditions (13), by implementing the conditions presented in Equation (14), can be written in the following form [50,62]:

$$\frac{\frac{\mu_{hnf}}{\mu_f}}{\frac{\rho_{hnf}}{\rho_f}} f''' + f''(g+f) - 2f'^2 - 2f'g' - \frac{\frac{\sigma_{hnf}}{\sigma_f}}{\frac{\rho_{hnf}}{\rho_f}} \frac{M}{1+m^2}(f' - mg') = 0, \tag{15}$$

$$\frac{\frac{\mu_{hnf}}{\mu_f}}{\frac{\rho_{hnf}}{\rho_f}} g''' + g''(g+f) - 2g'^2 - 2f'g' - \frac{\frac{\sigma_{hnf}}{\sigma_f}}{\frac{\sigma_{hnf}}{\sigma_f}} \frac{M}{1+m^2}(g' + mf') = 0, \tag{16}$$

$$\begin{aligned}\frac{\frac{k_{hnf}}{k_f}}{\frac{(\rho C_p)_{hnf}}{(\rho C_p)_f}} \frac{\theta''}{Pr} + \theta'(f+g) - a(f'+g')\theta + \epsilon_1[(\zeta(f'+g') + (2a+1)(f+g))(f'+g')\theta'\\ -a((a+2)(f'+g')^2 - (f''+g'')(f+g))\theta - (f+g)^2\theta''] + Nb\theta'\phi' + Nt\theta'^2 = 0,\end{aligned} \tag{17}$$

$$\frac{\phi''}{Sc}+\frac{Nt}{Nb}\frac{\theta''}{Sc}+\phi'(f+g)-a(f'+g')\phi+\epsilon_2[(\zeta(f'+g')+(2a+1)(f+g))(f'+g')\phi' \\ -a((a+2)(f'+g')^2-(f''+g'')(f+g))\phi-(f+g)^2\phi'']=0, \tag{18}$$

With the B.Cs.:

$$f=0=g, f'=1, g'=\gamma_0, \theta=1, \phi=1 \text{ at } \zeta=0, \\ f'\to 0, g'\to, \theta\to 0, \phi\to 0 \quad \text{as} \quad \zeta\to\infty. \tag{19}$$

Here, $Pr=\frac{\nu_f}{\alpha_f}$ is the Prandtl number, $Nt=\frac{\tau D_T(T_w-T_\infty)}{\nu T_\infty}$ and $Nb=\frac{\tau D_B(C_w-C_\infty)}{\nu}$ are the thermophoretic and Brownian motion parameters, $\gamma_0=\frac{d}{c}$ is the stretching ratio, $Sc=\frac{\nu}{D_B}$ is the Schmidt number, $\epsilon_1=\Lambda_e a$ and $\epsilon_2=\Lambda_e a$ are the thermal relaxation parameters for the energy and mass fluxes, respectively, $M=\frac{2L\sigma_f B_0^2}{\rho C_p}$ is the magnetic parameter, m is the Hall parameter, and μ_{hnf}, ρ_{hnf}, and $(\rho C_p)_{hnf}$ show the hybrid nanofluid dynamic viscosity, density, and specific heat, respectively. The hybrid nanofluid models for the thermal and electrical conductivity, specific heat, density, and dynamic viscosity are defined as [63,64]:

$$\frac{k_{hnf}}{k_{bf}}=(1-\varphi_2)+2\varphi_2\Big(\frac{k_{m2}}{k_{m2}-k_{bf}}\Big)ln\Big(\frac{k_{m2}+k_{bf}}{2k_{bf}}\Big), \\ \frac{k_{bf}}{k_f}=(1-\varphi_1)+2\varphi_1\Big(\frac{k_{m1}}{k_{m1}-k_f}\Big)ln\Big(\frac{k_{m1}+k_f}{2k_f}\Big), \tag{20}$$

$$\frac{\sigma_{hnf}}{\sigma_{bf}}=\Big[1+\frac{3\Big(\frac{\sigma_{m2}}{\sigma_{bf}}-1\Big)\varphi_2}{\Big(\frac{\sigma_{m2}}{\sigma_{bf}}+2\Big)-\Big(\frac{\sigma_{m2}}{\sigma_{bf}}-1\Big)\varphi_2}\Big], \\ \frac{\sigma_{bf}}{\sigma_f}=\Big[1+\frac{3\Big(\frac{\sigma_{m1}}{\sigma_f}-1\Big)\varphi_1}{\Big(\frac{\sigma_{m1}}{\sigma_f}+2\Big)-\Big(\frac{\sigma_{m1}}{\sigma_f}-1\Big)\varphi_1}\Big], \tag{21}$$

$$\frac{(\rho C_p)_{hnf}}{(\rho C_p)_f}=\Big[(1-\varphi_2)\Big(1-\Big(1-\frac{(\rho C_p)_{m1}}{(\rho C_p)_f}\Big)\varphi_1\Big)+\varphi_2\frac{(\rho C_p)_{m2}}{(\rho C_p)_f}\Big], \tag{22}$$

$$\frac{\mu_{hnf}}{\mu_f}=\frac{1}{(1-\varphi_1)^{2.5}(1-\varphi_2)^{2.5}}, \tag{23}$$

$$\frac{\rho_{hnf}}{\rho_f}=\Big[(1-\varphi_2)\Big(1-\Big(1-\frac{\rho_{m1}}{\rho_f}\Big)\varphi_1\Big)+\varphi_2\frac{\rho_{m2}}{\rho_f}\Big]. \tag{24}$$

The basic engineering quantities of interest take the following forms:

$$Sh_x(Re_x)^{-1/2}=-\phi'(0), \tag{25}$$

$$Nu_x(Re_x)^{-1/2}=-\frac{k_{hnf}}{k_f}\theta'(0), \tag{26}$$

$$C_{fx}(2Re_x)^{1/2}=\frac{\mu_{hnf}}{\mu_f}f''(0), \tag{27}$$

$$C_{fy}(2Re_y)^{1/2}=\frac{\mu_{hnf}}{\mu_f}\Big(\frac{d}{c}\Big)^{-1.5}g''(0). \tag{28}$$

Here, $Re_x=\frac{u_w x}{\nu}$ and $Re_y=\frac{V_w y}{\nu}$ demonstrate the local Reynolds numbers. Table 1 was used in simulation of this work, where the basic physical and dynamical properties of the hybrid nanofluid used are presented.

Table 1. Some basic physical and dynamical properties of the nanofluid used in this work [65,66].

Properties	Ag	CuO	Kerosene Oil
$k\left(\frac{W}{mK}\right)$	429	18	0.145
$C_p\left(\frac{J}{kgK}\right)$	235	540	2090
$\rho\left(\frac{kg}{m^3}\right)$	10,500	6500	783

3. Problem Solution by Homotopy Analysis Method

In this section, we solve the reduced system of ODEs together with the boundary conditions defined in Equations (15)–(19). These problems are normally very highly nonlinear, and that is one of the reasons that researchers use the semi-analytical techniques for solution purposes. One of the techniques we use here is the homotopy analysis method (HAM) introduced by Liao [67]. Liao used the concept of topology by constructing a continuous mapping between two functions $\xi_1(\bar{x})$ and $\xi_2(\bar{x})$, which are themselves continuous, defined over the two topological spaces $\bar{X}$ and $\bar{Y}$, on which this mapping is constructed. This mapping is mathematically defined as [68]:

$$\tilde{\Phi} : \bar{X} \times [0,1] \to \bar{Y}, \tag{29}$$

where $\tilde{\Phi}[\bar{X},0] = \xi_1(\bar{X})$ and $\tilde{\Phi}[\bar{X},1] = \xi_2(\bar{X})$ hold $\forall \bar{x} \in \bar{X}$.

Now, to solve Equations (15)–(18) together with the boundary conditions (19), we chose $f_0 = -\exp(-\zeta) + 1$, $g_0 = \gamma_0(-\exp(-\zeta) + 1)$, $\theta_0 = \exp(-\zeta)$, and $\phi_0 = \exp(-\zeta)$ as the initial guesses with the corresponding operators, defined as:

$$L_{\bar{f}}(\bar{f}) = \bar{f}''' - \bar{f}',\ L_{\bar{g}}(\bar{g}) = \bar{g}''' - \bar{g}',\ L_{\bar{\theta}}(\bar{\theta}) = \bar{\theta}'' - \bar{\theta},\ \text{and}\ L_{\bar{\phi}}(\bar{\phi}) = \bar{\phi}'' - \bar{\phi}, \tag{30}$$

which agree with

$$\begin{aligned} L_{\bar{f}}(a_1 + a_2\exp(\zeta) + a_3\exp(-\zeta)) = 0,\ L_{\bar{g}}(a_4 + a_5\exp(\zeta) + a_6\exp(-\zeta)) = 0, \\ L_{\bar{\theta}}(a_7\exp(\zeta) + a_8\exp(-\zeta)) = 0, L_{\bar{\phi}}(a_9\exp(\zeta) + a_{10}\exp(-\zeta)) = 0, \end{aligned} \tag{31}$$

where $a_i, i = 1 \to 10$ are arbitrary constants.

3.1. Convergence Analysis

In this section, we briefly explain the convergence of the method used in Section 3. For this purpose, we present the residual errors computed for the state variables in the form of Table 2. The residuals were computed subject to variations in the convergence control parameters used in the homotopy. These parameters are $\hbar_f$, $\hbar_g$, $\hbar_\theta$, and $\hbar_\phi$ and were chosen in such away that the square residual is minimized. Using the concept of Liao [69], the mathematical relations for the square residuals take the following forms:

$$\epsilon_f = \frac{1}{p+1}\sum_{l=0}^{p}\left[\mathcal{N}_f\Big(\sum_{r=0}^{n}\bar{f}(\zeta)\sum_{r=0}^{n}\bar{g}(\zeta)\Big)_{l\Delta\zeta}\right]^2, \tag{32}$$

$$\epsilon_g = \frac{1}{p+1}\sum_{l=0}^{p}\left[\mathcal{N}_g\Big(\sum_{r=0}^{n}\bar{f}(\zeta)\sum_{r=0}^{n}\bar{g}(\zeta)\Big)_{l\Delta\zeta}\right]^2, \tag{33}$$

$$\epsilon_\theta = \frac{1}{p+1}\sum_{l=0}^{p}\left[\mathcal{N}_\theta\Big(\sum_{r=0}^{n}\bar{f}(\zeta)\sum_{r=0}^{n}\bar{g}(\zeta)\sum_{r=0}^{n}\bar{\theta}(\zeta)\Big)_{l\Delta\zeta}\right]^2, \tag{34}$$

$$\epsilon_\phi = \frac{1}{p+1}\sum_{l=0}^{p}\left[\mathcal{N}_\phi\Big(\sum_{r=0}^{n}\bar{f}(\zeta)\sum_{r=0}^{n}\bar{g}(\zeta)\sum_{r=0}^{n}\bar{\theta}(\zeta)\sum_{r=0}^{n}\bar{\phi}(\zeta)\Big)_{l\Delta\zeta}\right]^2. \tag{35}$$

The total residual can be obtained from the following empirical relation by combining Equations (32)–(35), and we have [69]:

$$\epsilon_s = \epsilon_f + \epsilon_g + \epsilon_\theta + \epsilon_\phi. \tag{36}$$

In Equation (36), ϵ_s shows the sum of the residuals obtained. For the second-order deformation, we chose $\Delta\zeta = 0.45$ and $p = 20$ for the convergence control parameters $\hbar_f = -2.21453$, $\hbar_g = -2.56672$, $\hbar_\theta = -1.56345$, and $\hbar_\phi = -1.56345$. In Table 2, the various residuals computed are presented for the corresponding state variables. From the table, it is clear that, when the number of iterations increases, the residual error decreases.

Table 2. Squared residual error values subject to the auxiliary variables' values.

n	ϵ_f	ϵ_g	ϵ_θ	ϵ_ϕ
2	5.26×10^{-4}	4.34×10^{-5}	5.78×10^{-4}	5.78×10^{-4}
5	6.31×10^{-5}	2.49×10^{-6}	4.87×10^{-5}	4.87×10^{-5}
10	5.47×10^{-5}	6.91×10^{-6}	3.14×10^{-5}	3.14×10^{-5}
15	6.69×10^{-6}	8.76×10^{-7}	5.43×10^{-6}	5.43×10^{-6}
20	7.98×10^{-6}	4.28×10^{-7}	4.90×10^{-6}	4.90×10^{-6}
25	6.27×10^{-7}	3.76×10^{-8}	5.67×10^{-7}	5.67×10^{-7}
30	4.14×10^{-7}	2.93×10^{-8}	3.49×10^{-7}	3.49×10^{-7}

4. Results and Discussion

The results obtained by implementing the HAM in the above equations are presented in the form of graphs and tables in this section. The graphical description in Figures 2–17 expressed here shows the impact of various parameters on the state variables. Furthermore, the engineering quantities of interest are expressed in Tables 3 and 4.

The impact of the mass flux S_0 in the velocity $f'(\zeta)$ of the considered nanofluid (CuO+kerosene oil) and the hybrid nanofluid (Ag+CuO+kerosene oil) is depicted in Figure 2. The values of S_0 were taken to be $0.2, 0.4, 0.6$. The graph displays a decreasing dependence of the fluid velocity with increasing S_0. Both fluids exhibit almost the same dependence. Thus, the increasing S_0 causes a lower distribution in $f'(\zeta)$.

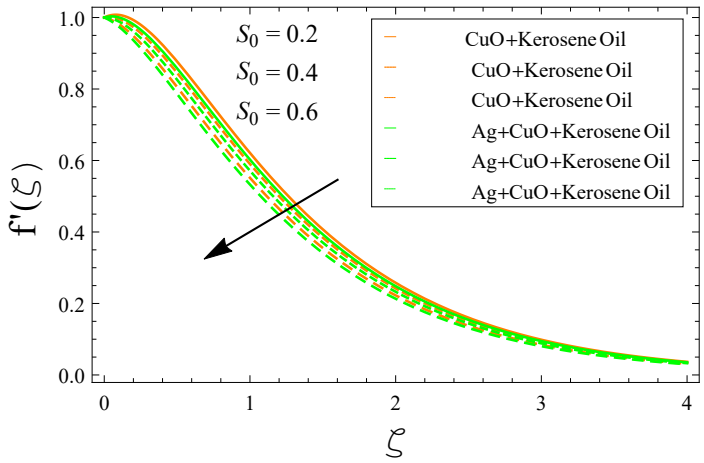

Figure 2. Influence of S_0 on $f'(\zeta)$.

The dependence of both nanofluids' dynamics on the varying magnetic field strength M is displayed in Figure 3. The graph shows that the increasing magnetic field strength M results in a reduction in the $f'(\zeta)$ profile. The values of M were taken to be $0.2, 0.4, 0.6$. The drop in $f'(\zeta)$ is more prominent at the intermediate values of ζ. The spacing between different curves decreases with the increasing values of M. The increasing M values causes $f'(\zeta)$ to reduce at a greater rate in the hybrid nanofluid compared to the ordinary

nanofluid. This shows that the increasing M values result in a reduction of the fluid velocity distribution.

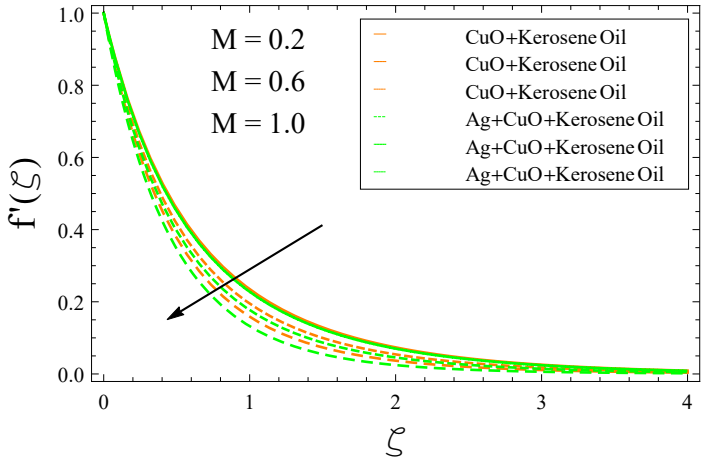

Figure 3. Influence of M on $f^{'}(\zeta)$.

The dependence of $f^{'}(\zeta)$ on the Hall effect parameter m is depicted in Figure 4. The chosen values of m were 0.2, 0.6, 0.9. The graph shows that the increasing values of m increase the profile of $f^{'}(\zeta)$ for both types of nanofluid. The increase is more prominent at the middle values of ζ. The increase in the hybrid nanofluid is the largest one for the highest of m, that is at $m = 0.9$. This shows that the increasing Hall effect strength results an increase in the velocity distribution of both types of nanofluid.

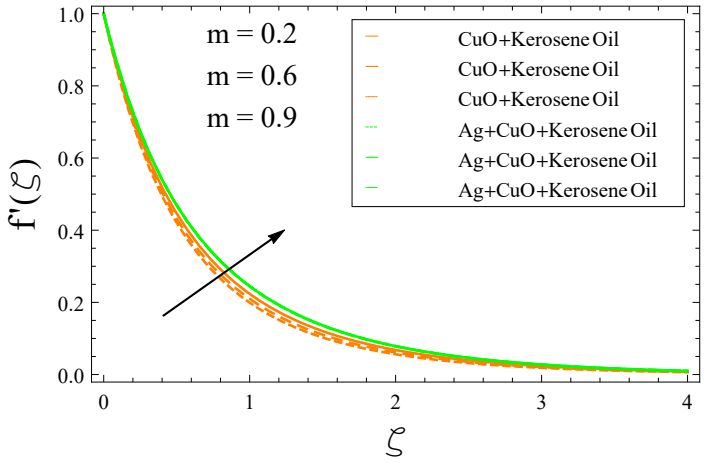

Figure 4. Dependence of $f^{'}(\eta)$ on m.

The impact of the stretching ratio γ_0 on the velocity distribution $f^{'}(\zeta)$ is plotted in Figure 5. The chosen values of γ_0 were 0.2, 0.6, 0.8. It is apparent that the changing of the γ_0 strength results in an increase in $f^{'}(\zeta)$. The increasing γ increases the velocity distribution of the simple nanofluid at a higher rate compared to the chosen hybrid nanofluid. The increase is more obvious at the intermediate values of γ_0.

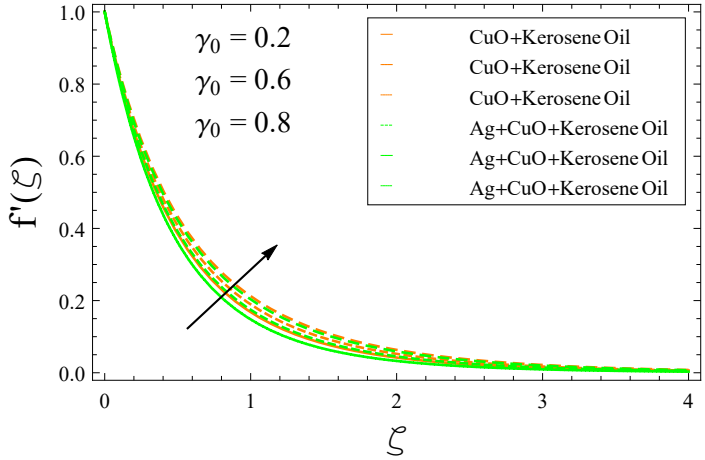

Figure 5. Variation of $f^{'}(\eta)$ with γ_0.

The impacts of the mass flux parameter S_0 and stretching ratio γ_0 on the other component of the velocity $g^{'}(\zeta)$ are respectively exhibited in Figures 6 and 7. The chosen values of S_0 were $0.1, 0.3, 0.5$, and those of γ_0 were $0.2, 0.6, 0.8$. It is clear from Figure 6 that the increasing mass flux causes the velocity distribution to reduce along the vertical direction. The drop is more drastic for the hybrid nanofluid compared to the simple nanofluid. The increasing stretching ratio strength γ_0 causes the velocity distribution to increase along the vertical direction, as displayed in Figure 7. The increase in the velocity distribution is more prominent for the hybrid nanofluid compared to the ordinary nanofluid. The spacing between different curves changes with the higher values of γ_0 at the intermediate values of ζ.

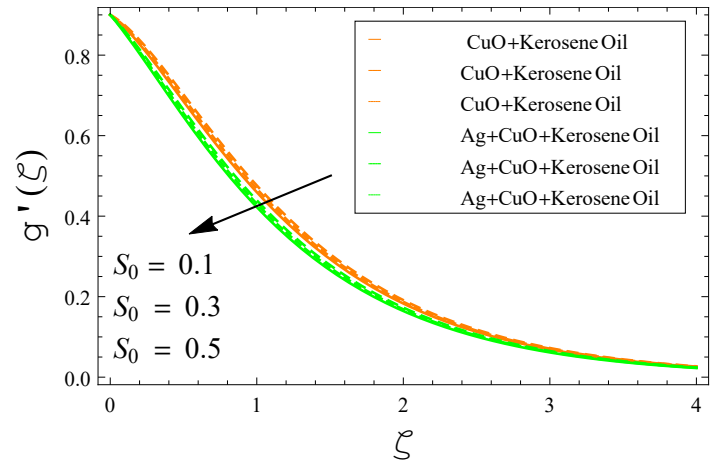

Figure 6. Impact of S_0 on $g^{'}(\zeta)$.

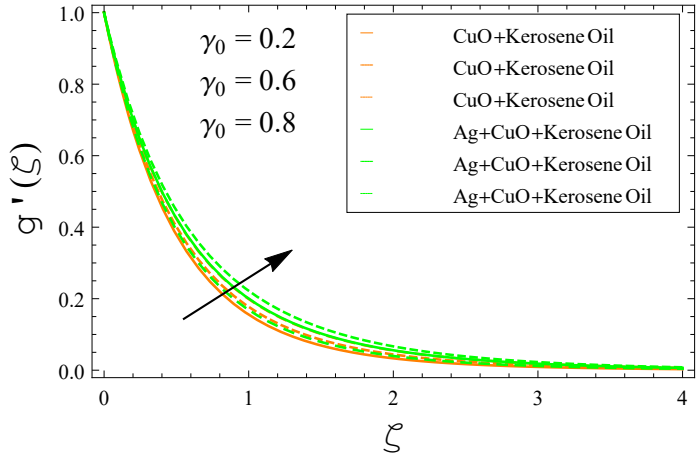

Figure 7. Dependence of $g^{'}(\zeta)$ on γ_0.

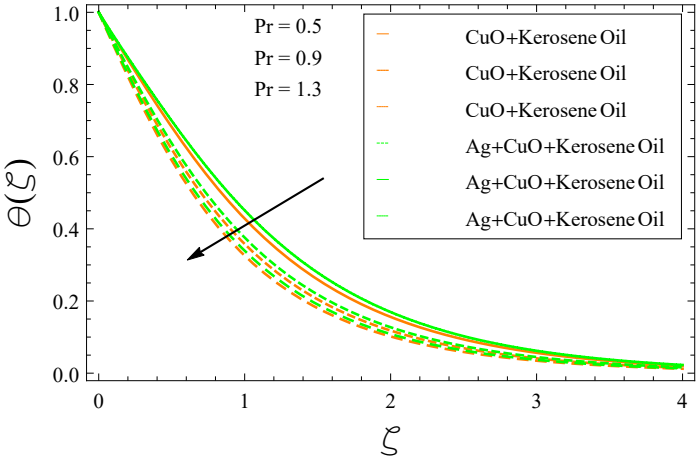

Figure 8. Variations in $\theta(\zeta)$ with Pr.

The dependence of the chosen simple and hybrid nanofluids temperature $\theta(\zeta)$ on Prandtl number Pr and thermophoresis parameter Nt is respectively plotted in Figures 8 and 9. The values of both parameters were chosen to be $0.5, 0.9, 1.3$. The temperature of both fluids drops with the increasing values of Pr. This is due to the thermal diffusion, because it has an inverse relation with Pr. On the other hand, when the viscous diffusion increases, the Prandtl number jumps up. As a result, the temperature profile decreases. The temperature drop shows a complex dependence on the increasing Pr. At a smaller value of Pr, the simple nanofluid temperature drops at a higher rate compared to the hybrid nanofluid temperature drop. At higher values, the temperature drop decreases compared to the smaller separation between the different curves. Thus, the smaller thermal diffusivity associated with a higher Pr results in a decrease in the temperature distribution of both types of fluid. Figure 9 shows that the changing thermophoresiscauses the temperature of the fluids to increase. The increasing nature of the fluids' temperature with the increasing Nt is higher for the hybrid nanofluid compared to the single-component nanofluid.

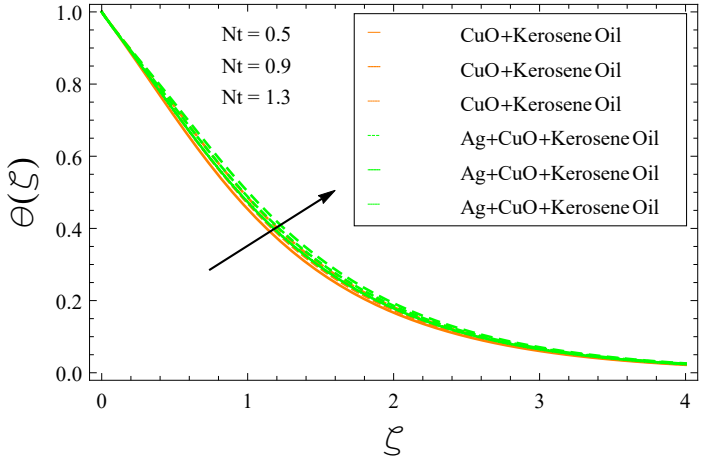

Figure 9. Impact of Nt on $\theta(\zeta)$.

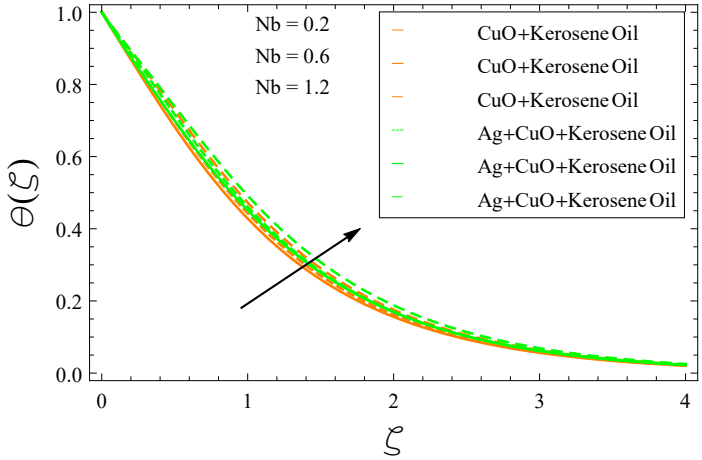

Figure 10. $\theta(\zeta)$ versus Nb.

The variation of the fluids' temperature with the changing Brownian motion parameter Nb, stretching ratio γ_0, and thermal energy relaxation parameter ϵ_1 is displayed in Figures 10–12, respectively. Figure 10 shows that the increasing randomness associated with the higher values of Nb causes the fluids' temperature to change. The rate of increase of the hybrid nanofluid is higher with the increasing Nb compared to the ordinary nanofluid. The increasing stretching ratio strength associated with the higher γ_0 decreases the fluid temperature, as exhibited in Figure 11. The dropping rate for both fluids almost shows the same trend. The reduction in the fluid temperature is more drastic at the intermediate values of ζ. The thermal energy relaxation exhibited by the increasing values of ϵ_1 also results in the reduction of the fluid temperature distribution $\theta(\zeta)$. The temperature dropping rate is higher for the hybrid nanofluid compared to the ordinary nanofluid. This is more obvious at the middle values of ζ. Thus, the increasing thermal energy relaxation causes the temperature distribution to reduce.

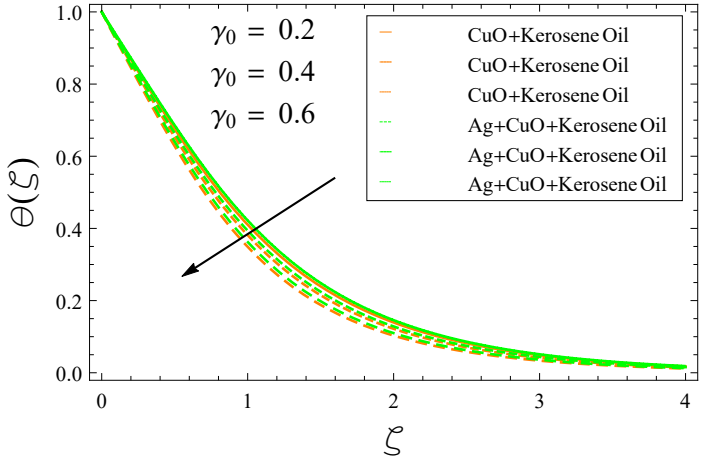

Figure 11. Dependence of $\theta(\zeta)$ on γ_0.

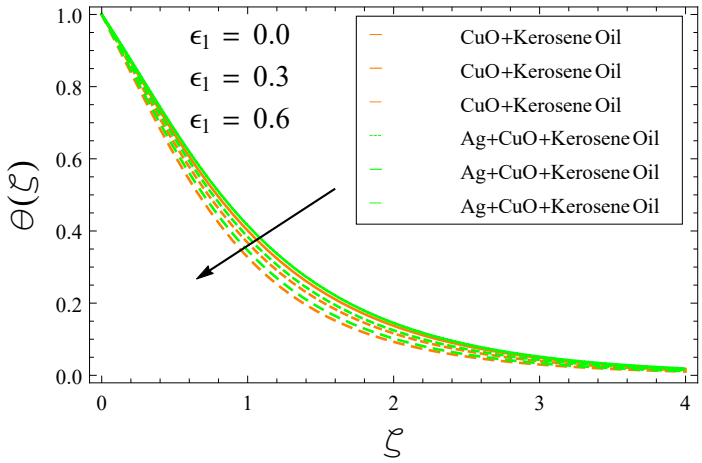

Figure 12. Influence of ϵ_1 on $\theta(\zeta)$.

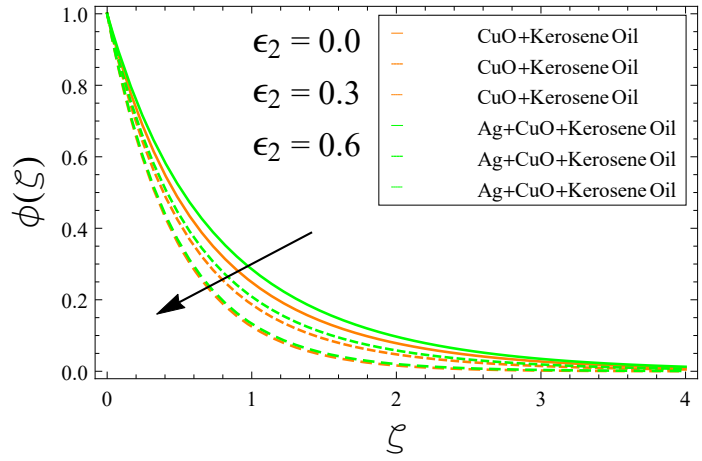

Figure 13. Influence of ϵ_2 on $\phi(\zeta)$.

The variation of the fluid concentration with the changing values of the mass flux relaxation parameter ϵ_2 and stretching ratio γ_0 are plotted respectively in Figures 13 and 14. The values of ϵ_2 were chosen to be $0.0, 0.3, 0.6$, whereas those of γ_0 were taken to be $0.2, 0.4, 0.6$. The changing mass flux relaxation drops the fluids' temperature. Initially, the dropping rate for the ordinary nanofluid is higher. As the values of ϵ_2 increase, the dropping rate decreases, as is clear from the reducing separation between the different curves.

At the highest ϵ_2, the concentration profiles for both fluids almost coincide. The drop in the fluids' concentration is more visible at the middle values of ζ. The increasing stretching ratio γ_0 also results in a reduction in the fluids' concentration, as shown in Figure 14. The drop in the hybrid nanofluid concentration is more obvious compared to the ordinary nanofluid.

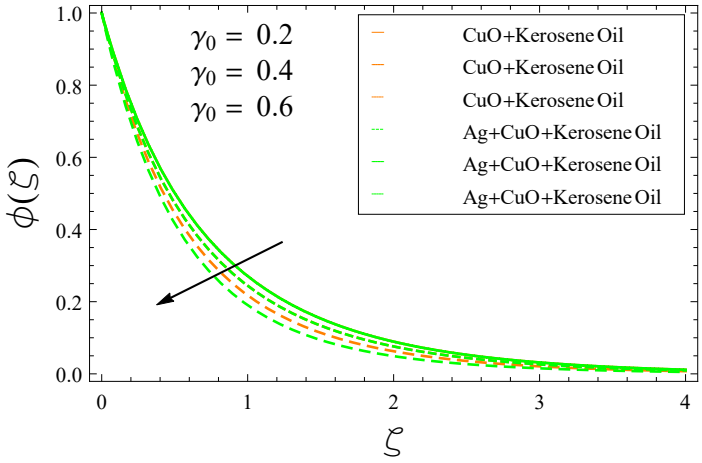

Figure 14. Influence of γ_0 on $\phi(\zeta)$.

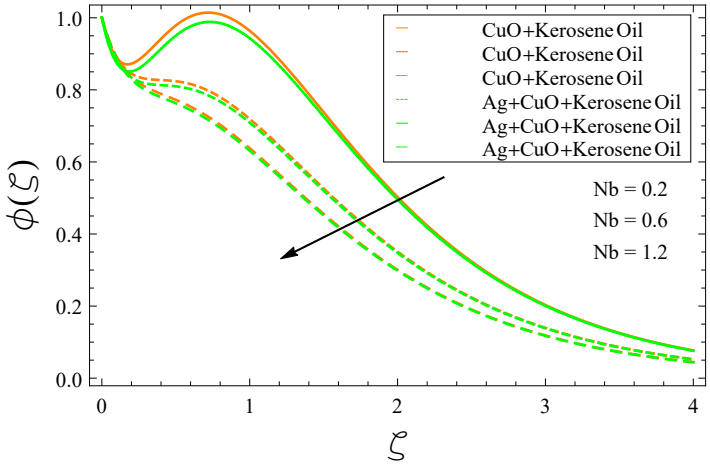

Figure 15. Influence of Nb on $\phi(\zeta)$.

The dependence of the fluid concentration ϕ on the increasing strength of Nb, Nt, and the Schmidt number Sc is respectively plotted in Figures 15–17. Figure 15 displays a strange dependence of the fluid concentration on Nb. The chosen values of Nb were $0.2, 0.6, 1.2$. At smaller ζ, the fluid concentration first drops, then rises with increasing ζ and reaches a maximum, then drops again with higher values of ζ. The rate of the concentration drop decreases with the increasing strength of the randomness associated with the higher Nb values, as exhibited by the decreasing separation between the different curves. The changing thermophoresis associated with the higher values of Nt causes the fluid concentration to change. The increasing rate of the fluid concentration is more prominent up to about $\zeta = 3.0$. Thus, the increasing thermophoresis affects the hybrid nanofluid concentration more drastically compared to the ordinary fluid. The impact of the increasing Schmidt number Sc on the fluid concentration $\phi(\zeta)$ is displayed in Figure 17. The chosen values of Sc were $0.6, 1.2, 1.8$. The graph exhibits a drop in the concentration profiles of both fluids. The rate of decrease of the ordinary nanofluid is more drastic with the increasing Sc compared to the hybrid nanofluid. Thus, the increasing kinematic viscosity associated with higher values of Sc affects the concentration profile of the ordinary

nanofluid more drastically compared to the hybrid nanofluid. The variation is more prominent at the intermediate values of ζ.

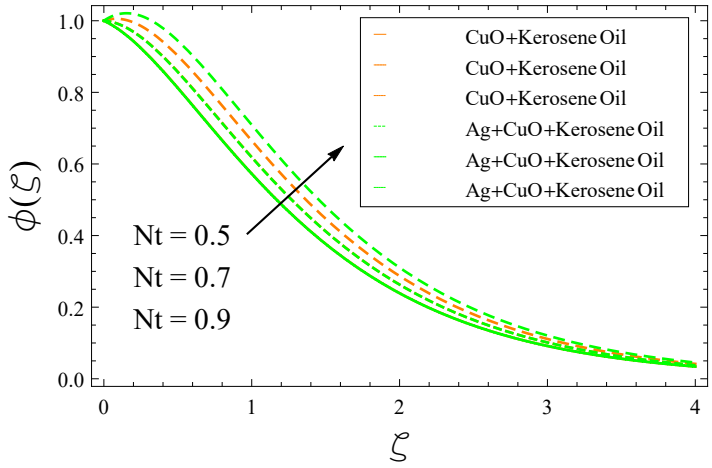

Figure 16. Influence of Nt on $\phi(\zeta)$.

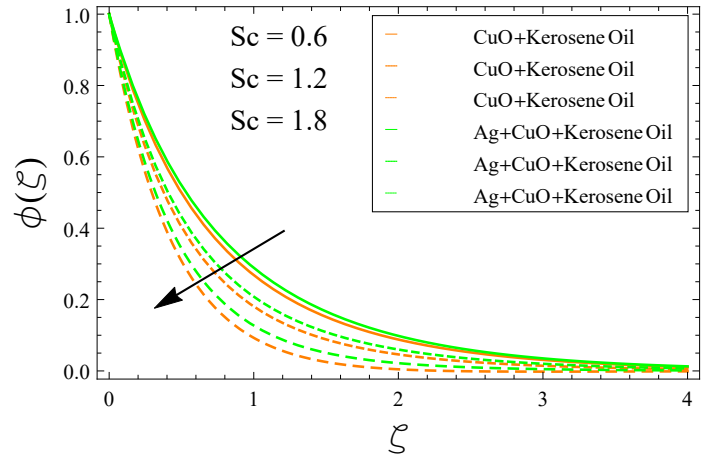

Figure 17. Influence of Sc on $\phi(\zeta)$.

Table 3. Computed values of C_{fx} and C_{fy}, under the variation of the ratio parameter (γ_0).

γ_0	0.2	0.4	0.6	0.8	1.0
C_{fx}	−1.04025	−1.07483	−1.09753	−1.11643	−1.16989
C_{fy}	−2.35546	−1.99025	−1.50623	−1.31678	−1.17889

Table 4. Computed values of the heat and mass transfer rate for various values of ϵ_1 and ϵ_2.

ϵ_1, ϵ_2	0.0	0.2	0.4	0.6	0.8
$\theta'(0)$	−0.52003	−0.52098	−0.52941	−0.53452	−0.53742
$\phi'(0)$	−0.51341	−0.51661	−0.51946	−0.52367	−0.53854

5. Tables' Discussion

In this section, various coefficients of engineering interest are displayed in Tables 3 and 4 numerically. The variations of these coefficients were analyzed under the variations of the ratio parameter γ, thermal relaxation parameter ϵ_1, and concentration relaxation parameter ϵ_2. Table 3 shows the opposite behavior with the increasing values of the ratio parameter. In Table 4, the relaxation parameter of heat with increasing values shows that the heat

transfer is increasing. A quite similar trend for the mass transfer rate is observed in Table 4 for the mass relaxation parameter.

6. Conclusions

This section is concerned with the results obtained in this work. In this work, the CCDD model was used to simulate the Ag+CuO+kerosene oil hybrid nanofluid passing a bidirectionally stretching sheet, under the influence of the variable magnetic parameter. The fluid was chosen to be electrically conductive, where the current produced (Hall current) was taken into account. The results obtained through graphs and tables are summarized below:

- When the Hall current increases, the velocity gradient increases, while the dimensionless mass flux and the magnetic parameter decrease this profile.
- Both the velocity and temperature profiles fall with the increasing values of the ratio parameter.
- The higher values of the Prandtl number decrease the layer thickness of the thermal boundary.
- Both the temperature and concentration boundary layer show an opposite trend for the larger values of the Brownian motion parameter.
- The thermal and concentration parameters decrease the temperature and concentration boundary layers with their increasing values.
- At the surface, both the temperature and concentration profiles show an increasing trend for various values of the thermal and concentration boundary layers.
- The skin friction shows the opposite trend for the larger values of the ratio parameter γ_0.
- The graphs show that the hybrid nanofluid shows a fast increasing/decreasing trend, which implies further applications in cooling.
- The efficiency of the implemented technique is proven in Section 3.1 through the squared residual errors presented in Table 2.

Author Contributions: Conceptualization, H.A.E.-W.K., and A.U.; software, M.A., R.A.Z., and A.U.; writing—original draft preparation, A.U., R.A.Z., and H.A.E.-W.K.; writing—review and editing, H.A.E.-W.K., M.A., and A.U.; formal analysis, M.A., H.A.E.-W.K., and R.A.Z.; validation, H.A.E.-W.K., A.U., M.A., and R.A.Z.; methodology, A.U., M.A., and H.A.E.-W.K.; investigation, H.A.E.-W.K., M.A., and A.U.; resources, A.U., and R.A.Z.; project administration, A.U., and H.A.E.-W.K.; funding acquisition, R.A.Z., and H.A.E.-W.K. All authors have read and agreed to the published version of the manuscript.

Funding: This research work was funded by Institutional Fund projects under Grant No. (IFPIP: 1588-305-1443). The authors gratefully acknowledge the technical and financial support provided by the Ministry of Education and King Abdulaziz University, DSR, Jeddah, Saudi Arabia.

Data Availability Statement: The data used to support the findings of this study are available within the article.

Acknowledgments: This research work was funded by Institutional Fund projects under Grant No. (IFPIP: 1588-305-1443). The authors gratefully acknowledge the technical and financial support provided by the Ministry of Education and King Abdulaziz University, DSR, Jeddah, Saudi Arabia.

Conflicts of Interest: The authors declare no conflict of interest.

Abbreviations

σ	Electrical conductivity
C	Concentration
B	Uniform magnetic parameter strength T
Nu_x	Local Nusselt number
Re_x	Local Reynolds number
C_{fx},C_{fy}	Local skin frictions
Sh_x	Sherwood number along the x-axis
Pr	Prandtl number
u_w	Stretching velocity along the x-axis
v_w	Stretching velocity along the y-axis
T	Fluid temperature (K)
θ	Dimensionless temperature
f	Dimensionless velocity along the x-axis
g	Dimensionless velocity along the y-axis
θ	Dimensionless temperature
ϕ	Dimensionless concentration
ρ	Density
μ	Dynamic viscosity
C_p	Specific heat
$(C_p)_{hnf}$	Hybrid nanofluid specific heat
μ_{hnf}	Hybrid nanofluid dynamic viscosity
ρ_{hnf}	Hybrid nanofluid density
J_w	Mass flux
∞	Condition at infinity
0	Reference condition
w	Condition at the wall
x, y, and z	Coordinates
ζ	Similarity variable
γ_0	Stretching ratio parameter
Sc	Schmidt number
t	Time (s)
k_{hnf}	Hybrid nanofluid thermal conductivity
k_{bf}	Base fluid thermal conductivity
σ_{bf}	Base fluid electrical conductivity
σ_{hnf}	Hybrid nanofluid electrical conductivity
M	Magnetic parameter
m	Hall parameter
$\tilde{V}$	Velocity field
$\tilde{q}$	Heat flux
$\tilde{j}$	Mass flux
Λ_e	Energy relaxation parameter
c, d	References of velocity
L	Characteristic length
$B(x, y)$	Variable magnetic field
B_0	Strength of the magnetic field
Λ_c	Concentration relaxation parameter
D_B	Brownian motion parameter
τ	Adiabatic index
S_0	Suction/injection parameter
N_t	Thermo-migration parameter
ϵ_1	Thermal relaxation parameter
ϵ_2	Mass relaxation parameter
D_T	Thermophoretic parameter

References

1. Choi, S.U.; Eastman, J.A. *Enhancing Thermal Conductivity of Fluids with Nanoparticles*; Technical report; Argonne National Lab.(ANL): Argonne, IL, USA, 1995.
2. Eastman, J.A.; Choi, S.; Li, S.; Yu, W.; Thompson, L. Anomalously increased effective thermal conductivities of ethylene glycol-based nanofluids containing copper nanoparticles. *Appl. Phys. Lett.* **2001**, *78*, 718–720. [CrossRef]
3. Maïga, S.E.B.; Nguyen, C.T.; Galanis, N.; Roy, G. Heat transfer behaviors of nanofluids in a uniformly heated tube. *Superlattices Microstruct.* **2004**, *35*, 543–557. [CrossRef]
4. Khan, W.; Pop, I. Boundary-layer flow of a nanofluid past a stretching sheet. *Int. J. Heat Mass Transf.* **2010**, *53*, 2477–2483. [CrossRef]
5. Seth, G.; Kumar, B.; Nandkeolyar, R. MHD mixed convection stagnation point flow of a micropolar nanofluid adjacent to stretching sheet: A revised model with successive linearization method. *J. Nanofluids* **2019**, *8*, 620–630. [CrossRef]
6. Rashidi, M.M.; Ghahremanian, S.; Toghraie, D.; Roy, P. Effect of solid surface structure on the condensation flow of Argon in rough nanochannels with different roughness geometries using molecular dynamics simulation. *Int. Commun. Heat Mass Transf.* **2020**, *117*, 104741. [CrossRef]
7. Mansoury, D.; Ilami Doshmanziari, F.; Rezaie, S.; Rashidi, M.M. Effect of Al_2O_3/water nanofluid on performance of parallel flow heat exchangers. *J. Therm. Anal. Calorim.* **2019**, *135*, 625–643. [CrossRef]
8. Hatami, M.; Zhou, J.; Geng, J.; Song, D.; Jing, D. Optimization of a lid-driven T-shaped porous cavity to improve the nanofluids mixed convection heat transfer. *J. Mol. Liq.* **2017**, *231*, 620–631. [CrossRef]
9. Jana, S.; Salehi-Khojin, A.; Zhong, W.H. Enhancement of fluid thermal conductivity by the addition of single and hybrid nano-additives. *Thermochim. Acta* **2007**, *462*, 45–55. [CrossRef]
10. Madhesh, D.; Parameshwaran, R.; Kalaiselvam, S. Experimental investigation on convective heat transfer and rheological characteristics of Cu–TiO_2 hybrid nanofluids. *Exp. Therm. Fluid Sci.* **2014**, *52*, 104–115. [CrossRef]
11. Ho, C.; Huang, J.; Tsai, P.; Yang, Y. Preparation and properties of hybrid water-based suspension of Al_2O_3 nanoparticles and MEPCM particles as functional forced convection fluid. *Int. Commun. Heat Mass Transf.* **2010**, *37*, 490–494. [CrossRef]
12. Suresh, S.; Venkitaraj, K.; Selvakumar, P.; Chandrasekar, M. Synthesis of Al_2O_3–Cu/water hybrid nanofluids using two step method and its thermo physical properties. *Colloids Surfaces A: Physicochem. Eng. Asp.* **2011**, *388*, 41–48. [CrossRef]
13. Labib, M.N.; Nine, M.J.; Afrianto, H.; Chung, H.; Jeong, H. Numerical investigation on effect of base fluids and hybrid nanofluid in forced convective heat transfer. *Int. J. Therm. Sci.* **2013**, *71*, 163–171. [CrossRef]
14. Moghadassi, A.; Ghomi, E.; Parvizian, F. A numerical study of water based Al_2O_3 and Al_2O_3–Cu hybrid nanofluid effect on forced convective heat transfer. *Int. J. Therm. Sci.* **2015**, *92*, 50–57. [CrossRef]
15. Daniel, Y.S.; Aziz, Z.A.; Ismail, Z.; Salah, F. Thermal radiation on unsteady electrical MHD flow of nanofluid over stretching sheet with chemical reaction. *J. King Saud Univ.-Sci.* **2019**, *31*, 804–812. [CrossRef]
16. Khan, I. Shape effects of MoS2 nanoparticles on MHD slip flow of molybdenum disulphide nanofluid in a porous medium. *J. Mol. Liq.* **2017**, *233*, 442–451. [CrossRef]
17. Chamkha, A.J.; Ismael, M.A. Magnetic field effect on mixed convection in lid-driven trapezoidal cavities filled with a Cu–water nanofluid with an aiding or opposing side wall. *J. Therm. Sci. Eng. Appl.* **2016**, *8*, 031009. [CrossRef]
18. Alsabery, A.I.; Ismael, M.A.; Chamkha, A.J.; Hashim, I. Mixed convection of Al_2O_3-water nanofluid in a double lid-driven square cavity with a solid inner insert using Buongiorno's two-phase model. *Int. J. Heat Mass Transf.* **2018**, *119*, 939–961. [CrossRef]
19. Ellahi, R. The effects of MHD and temperature dependent viscosity on the flow of non-Newtonian nanofluid in a pipe: Analytical solutions. *Appl. Math. Model.* **2013**, *37*, 1451–1467. [CrossRef]
20. Sheikholeslami, M.; D Ganji, D. Magnetohydrodynamic flow in a permeable channel filled with nanofluid. *Sci. Iran.* **2014**, *21*, 203–212.
21. Seyyedi, S.M.; Dogonchi, A.; Hashemi-Tilehnoee, M.; Asghar, Z.; Waqas, M.; Ganji, D. A computational framework for natural convective hydromagnetic flow via inclined cavity: An analysis subjected to entropy generation. *J. Mol. Liq.* **2019**, *287*, 110863. [CrossRef]
22. Rashidi, M.; Abelman, S.; Mehr, N.F. Entropy generation in steady MHD flow due to a rotating porous disk in a nanofluid. *Int. J. Heat Mass Transf.* **2013**, *62*, 515–525. [CrossRef]
23. Sheikholeslami, M.; Ellahi, R. Three dimensional mesoscopic simulation of magnetic field effect on natural convection of nanofluid. *Int. J. Heat Mass Transf.* **2015**, *89*, 799–808. [CrossRef]
24. Biswas, N.; Mandal, D.K.; Manna, N.K.; Benim, A.C. Enhanced energy and mass transport dynamics in a thermo-magneto-bioconvective porous system containing oxytactic bacteria and nanoparticles: Cleaner energy application. *Energy* **2023**, *263*, 125775. [CrossRef]
25. Manna, N.K.; Biswas, N.; Mandal, D.K.; Sarkar, U.; Öztop, H.F.; Abu-Hamdeh, N. Impacts of heater-cooler position and Lorentz force on heat transfer and entropy generation of hybrid nanofluid convection in quarter-circular cavity. *Int. J. Numer. Methods Heat Fluid Flow* 2022, *ahead-of-print*. [CrossRef]
26. Biswas, N.; Mondal, M.K.; Manna, N.K.; Mandal, D.K.; Chamkha, A.J. Implementation of partial magnetic fields to magneto-thermal convective systems operated using hybrid-nanoliquid and porous media. *Proc. Inst. Mech. Eng. Part C J. Mech. Eng. Sci.* **2022**, *236*, 5687–5704. [CrossRef]

27. Mandal, D.K.; Biswas, N.; Manna, N.K.; Gorla, R.S.R.; Chamkha, A.J. Hybrid nanofluid magnetohydrodynamic mixed convection in a novel W-shaped porous system. *Int. J. Numer. Methods Heat Fluid Flow* 2022, *ahead-of-print*. [CrossRef]
28. Biswas, N.; Mandal, D.K.; Manna, N.K.; Benim, A.C. Magneto-hydrothermal triple-convection in a W-shaped porous cavity containing oxytactic bacteria. *Sci. Rep.* **2022**, *12*, 1–30. [CrossRef] [PubMed]
29. Mandal, D.K.; Biswas, N.; Manna, N.K.; Gayen, D.K.; Gorla, R.S.R.; Chamkha, A.J. Thermo-fluidic transport process in a novel M-shaped cavity packed with non-Darcian porous medium and hybrid nanofluid: Application of artificial neural network (ANN). *Phys. Fluids* **2022**, *34*, 033608. [CrossRef]
30. Mandal, D.; Biswas, N.; Manna, N.; Gorla, R. Magneto-thermal convection of hybrid nanofluid in a non-Darcian porous complex wavy enclosure. *Eur. Phys. J. Spec. Top.* **2022**, *213*, 2695–2712 [CrossRef]
31. Sakiadis, B.C. Boundary-layer behavior on continuous solid surfaces: I. Boundary-layer equations for two-dimensional and axisymmetric flow. *AIChE J.* **1961**, *7*, 26–28. [CrossRef]
32. Sakiadis, B. Boundary-layer behavior on continuous solid surfaces: II. The boundary layer on a continuous flat surface. *AiChE J.* **1961**, *7*, 221–225. [CrossRef]
33. Sakiadis, B. Boundary-layer behavior on continuous solid surfaces: III. The boundary layer on a continuous cylindrical surface. *AiChE J.* **1961**, *7*, 467–472. [CrossRef]
34. Crane, L.J. Flow past a stretching plate. *Z. Angew. Math. Phys. ZAMP* **1970**, *21*, 645–647. [CrossRef]
35. Gupta, P.; Gupta, A. Heat and mass transfer on a stretching sheet with suction or blowing. *Can. J. Chem. Eng.* **1977**, *55*, 744–746. [CrossRef]
36. Devi, R.; Neeraja, A.; Reddy, N.B. Radiation effect on MHD slip flow past a stretching sheet with variable viscosity and heat source/sink. *Int. J. Sci. Innov. Math. Res.* **2015**, *3*, 8–17.
37. Magyari, E.; Keller, B. Heat and mass transfer in the boundary layers on an exponentially stretching continuous surface. *J. Phys. D: Appl. Phys.* **1999**, *32*, 577. [CrossRef]
38. Wang, C. Liquid film on an unsteady stretching surface. *Q. Appl. Math.* **1990**, *48*, 601–610. [CrossRef]
39. Miklavčič, M.; Wang, C. Viscous flow due to a shrinking sheet. *Q. Appl. Math.* **2006**, *64*, 283–290. [CrossRef]
40. Bhattacharyya, K. Boundary layer flow and heat transfer over an exponentially shrinking sheet. *Chin. Phys. Lett.* **2011**, *28*, 074701. [CrossRef]
41. Bhattacharyya, K.; Vajravelu, K. Stagnation-point flow and heat transfer over an exponentially shrinking sheet. *Commun. Nonlinear Sci. Numer. Simul.* **2012**, *17*, 2728–2734. [CrossRef]
42. Bachok, N.; Ishak, A.; Pop, I. Boundary layer stagnation-point flow and heat transfer over an exponentially stretching/shrinking sheet in a nanofluid. *Int. J. Heat Mass Transf.* **2012**, *55*, 8122–8128. [CrossRef]
43. Sharma, R.; Ishak, A.; Nazar, R.; Pop, I. Boundary layer flow and heat transfer over a permeable exponentially shrinking sheet in the presence of thermal radiation and partial slip. *J. Appl. Fluid Mech.* **2014**, *7*, 125–134.
44. Jusoh, R.; Nazar, R.; Pop, I. Magnetohydrodynamic boundary layer flow and heat transfer of nanofluids past a bidirectional exponential permeable stretching/shrinking sheet with viscous dissipation effect. *J. Heat Transf.* **2019**, *141*, 012406. [CrossRef]
45. Dero, S.; Rohni, A.M.; Saaban, A. MHD micropolar nanofluid flow over an exponentially stretching/shrinking surface: Triple solutions. *J. Adv. Res. Fluid Mech. Therm. Sci.* **2019**, *56*, 165–174.
46. Lund, L.A.; Omar, Z.; Khan, I. Quadruple solutions of mixed convection flow of magnetohydrodynamic nanofluid over exponentially vertical shrinking and stretching surfaces: Stability analysis. *Comput. Methods Programs Biomed.* **2019**, *182*, 105044. [CrossRef] [PubMed]
47. Christov, C. On frame indifferent formulation of the Maxwell–Cattaneo model of finite-speed heat conduction. *Mech. Res. Commun.* **2009**, *36*, 481–486. [CrossRef]
48. Rauf, A.; Abbas, Z.; Shehzad, S. Utilization of Maxwell-Cattaneo law for MHD swirling flow through oscillatory disk subject to porous medium. *Appl. Math. Mech.* **2019**, *40*, 837–850. [CrossRef]
49. Sui, J.; Zheng, L.; Zhang, X. Boundary layer heat and mass transfer with Cattaneo–Christov double-diffusion in upper-convected Maxwell nanofluid past a stretching sheet with slip velocity. *Int. J. Therm. Sci.* **2016**, *104*, 461–468. [CrossRef]
50. Hayat, T.; Muhammad, T.; Alsaedi, A.; Ahmad, B. Three-dimensional flow of nanofluid with Cattaneo–Christov double diffusion. *Results Phys.* **2016**, *6*, 897–903. [CrossRef]
51. Hayat, T.; Aziz, A.; Muhammad, T.; Alsaedi, A. Model and comparative study for flow of viscoelastic nanofluids with Cattaneo–Christov double diffusion. *PLoS ONE* **2017**, *12*, e0168824. [CrossRef]
52. Hayat, T.; Qayyum, S.; Shehzad, S.A.; Alsaedi, A. Chemical reaction and heat generation/absorption aspects in flow of Walters-B nanofluid with Cattaneo–Christov double-diffusion. *Results Phys.* **2017**, *7*, 4145–4152. [CrossRef]
53. Hayat, T.; Aziz, A.; Muhammad, T.; Alsaedi, A. Three-dimensional flow of Prandtl fluid with Cattaneo–Christov double diffusion. *Results Phys.* **2018**, *9*, 290–296. [CrossRef]
54. Ibrahim, W. Three dimensional rotating flow of Powell-Eyring nanofluid with non-Fourier's heat flux and non-Fick's mass flux theory. *Results Phys.* **2018**, *8*, 569–577. [CrossRef]
55. Irfan, M.; Khan, M.; Khan, W. On model for three-dimensional Carreau fluid flow with Cattaneo–Christov double diffusion and variable conductivity: A numerical approach. *J. Braz. Soc. Mech. Sci. Eng.* **2018**, *40*, 1–10. [CrossRef]
56. Iqbal, Z.; Khan, M.; Ahmed, A.; Ahmed, J.; Hafeez, A. Thermal energy transport in Burgers nanofluid flow featuring the Cattaneo–Christov double diffusion theory. *Appl. Nanosci.* **2020**, *10*, 5331–5342. [CrossRef]

57. Ahmad, I.; Faisal, M.; Javed, T. Bi-directional stretched nanofluid flow with Cattaneo–Christov double diffusion. *Results Phys.* **2019**, *15*, 102581. [CrossRef]
58. Rauf, A.; Shehzad, S.; Abbas, Z.; Hayat, T. Unsteady three-dimensional MHD flow of the micropolar fluid over an oscillatory disk with Cattaneo–Christov double diffusion. *Appl. Math. Mech.* **2019**, *40*, 1471–1486. [CrossRef]
59. Fiza, M.; Alsubie, A.; Ullah, H.; Hamadneh, N.N.; Islam, S.; Khan, I. Three-dimensional rotating flow of MHD Jeffrey fluid flow between two parallel plates with impact of hall current. *Math. Probl. Eng.* **2021**, *2021*, 6626411. [CrossRef]
60. Shamshuddin, M.; Salawu, S.; Ogunseye, H.; Mabood, F. Dissipative power-law fluid flow using spectral quasi linearization method over an exponentially stretchable surface with Hall current and power-law slip velocity. *Int. Commun. Heat Mass Transf.* **2020**, *119*, 104933. [CrossRef]
61. Ramzan, M.; Gul, H.; Chung, J.D.; Kadry, S.; Chu, Y.M. Significance of Hall effect and Ion slip in a three-dimensional bioconvective Tangent hyperbolic nanofluid flow subject to Arrhenius activation energy. *Sci. Rep.* **2020**, *10*, 1–15. [CrossRef]
62. Zangooee, M.R.; Hosseinzadeh, K.; Ganj, D.D. Investigation of three-dimensional hybrid nanofluid flow affected by nonuniform MHD over exponential stretching/shrinking plate. *Nonlinear Eng.* **2022**, *11*, 143–155. [CrossRef]
63. Turkyilmazoglu, M.; Pop, I. Heat and mass transfer of unsteady natural convection flow of some nanofluids past a vertical infinite flat plate with radiation effect. *Int. J. Heat Mass Transf.* **2013**, *59*, 167–171. [CrossRef]
64. Turkyilmazoglu, M. On the transparent effects of Buongiorno nanofluid model on heat and mass transfer. *Eur. Phys. J. Plus* **2021**, *136*, 1–15. [CrossRef]
65. Algehyne, E.A.; Alharbi, A.F.; Saeed, A.; Dawar, A.; Ramzan, M.; Kumam, P. Analysis of the MHD partially ionized GO-Ag/water and GO-Ag/kerosene oil hybrid nanofluids flow over a stretching surface with Cattaneo–Christov double diffusion model: A comparative study. *Int. Commun. Heat Mass Transf.* **2022**, *136*, 106205. [CrossRef]
66. Ahmad, S.; Ali, K.; Ashraf, M.; Jamshed, W. Thermal Characteristics of Kerosene Oil based Hybrid Nanofluids (Ag-$MnZnFe_2O_4$): A Comprehensive Study. *Front. Energy Res.* **2022**, *10*, 978819. [CrossRef]
67. Liao, S.J. The Proposed Homotopy Analysis Technique for the Solution of Nonlinear Problems. Ph.D. Thesis, Shanghai Jiao Tong University, Shanghai, China, 1992.
68. Liao, S. Homotopy analysis method: A new analytical technique for nonlinear problems. *Commun. Nonlinear Sci. Numer. Simul.* **1997**, *2*, 95–100. [CrossRef]
69. Liao, S. An optimal homotopy-analysis approach for strongly nonlinear differential equations. *Commun. Nonlinear Sci. Numer. Simul.* **2010**, *15*, 2003–2016. [CrossRef]